Electronic Supplementary Material (ESI) for Nanoscale.
This journal is © The Royal Society of Chemistry 2024

Supplementary information

A. EUV-IL based on transmission gratings

In EUV-IL, an interference pattern created by two or more coherent beams is used to expose a photoresist. A synchrotron beamline (Fig. S1a) is an ideal light source for such systems. We use masks with transmission diffraction gratings that are fabricated on thin transparent membranes (Fig. S1b). The standing wave that results from the interference of two or more mutually coherent beams, generates a sinusoidal intensity variation that exposes the sample photoresist. In the simplest case of a two-beam interference (Fig. S1c), the light beam with wavelength λ passes through a mask that consists of two gratings with period g surrounded by a photonstop metal layer. Each order of diffraction m is deflected at a specific angle a_m with respect to the incident, given by the grating equation:

$$\sin a_m = \frac{m\lambda}{g} \tag{S1}$$

The interference period depends on the angle of the diffracted beams θ_m and is given by Eq. (S2). However, the latter is independent of the wavelength, because $\theta_m = 2\alpha_m$ and therefore Eq. (S1) & (S2) are combined in Eq. (S3).

$$P = \frac{\lambda/2}{\sin\left(\theta_m/2\right)} \tag{S2}$$

$$P = \frac{\lambda/2}{\sin a_m} = \frac{\lambda/2}{m\lambda/g} = \frac{g}{2m} \tag{S3}$$

Here, one can see the frequency multiplication, one of the main advantages of interference lithography. Our system utilizes the 1st order diffracted beams, because the diffraction efficiency of higher orders reduces dramatically, e.g. the 2nd order has almost 100x lower efficiency[1]. In 1st order diffraction shown in Fig. S1**c**, the patterning pitch is half of the one required to fabricate the used mask.

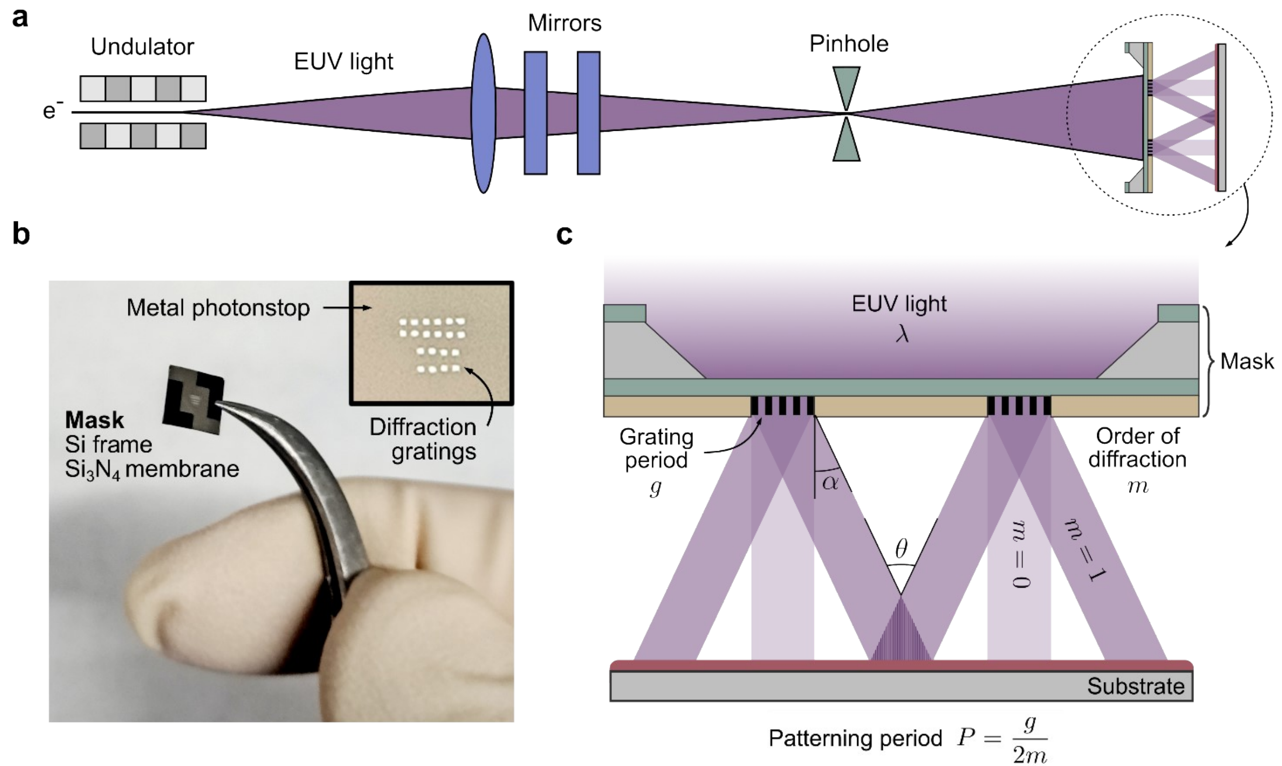

Fig. S1 | EUV interference lithography. (a) Schematic representation of the XIL-II beamline at the Paul Scherrer Institute. EUV light with tunable wavelength is generated by an undulator and gets reflected off a series of mirrors for high harmonic suppression and focusing. The beam is then focused on a pinhole (spatial filter) and the spatially coherent beam subsequently illuminates the imaging module (mask with gratings). (b) Photograph of a mask with transmission gratings. The spacing between the grating sets varies with their grating period in order to get the same mask-sample spacing for the different diffraction angles. (c) The operation principle of EUV-IL based on transmission gratings. A silicon nitride membrane (green) is grown and released by KOH-etching of the Si wafer (gray). Gratings with period g are formed on HSQ photoresist by EBL. The metal photonstop (beige) ensures that light passes only through the gratings where it gets diffracted. The interference pattern of the 1st order diffracted beams gets recorded on the sample photoresist (red) and its period is independent of the wavelength λ.

B. The period of a MIL exposure

The interference pattern intensity as a function of the mirror angle and the wavelength is given by Eq. (2)[2]. The pitch of a MIL exposure in Eq. (4),(S5) is derived by Eq. (2) using Euler's formula and trigonometric identities $\cos(\sin(-u)) = \cos(\sin(u))$ & $\sin(\sin(-u)) = -\sin(\sin(u))$, as following:

$$I(x) = A^2 \left| e^{i\frac{2\pi x}{\lambda} sin(2a)} + e^{i\frac{2\pi x}{\lambda} sin(-2a)} \right|^2$$

$$I(x) = 4A^2 \cos^2\left(\frac{2\pi x}{\lambda} sin(2a)\right)$$

$$I(x) = 2A^2\left(1 + cos\left(\frac{4\pi}{\lambda} sin(2a)\, x\right)\right). \tag{S4}$$

The frequency of the periodic Eq. (S4) is $f = (4\pi/\lambda)\sin 2\alpha$, therefore, the period $P = 2\pi/f$ is:

$$P = \frac{\lambda}{2\sin 2\alpha} \tag{S5}$$

The distance between the centers of the reflection and the overlap areas (Fig. 1b & S2a) is:

$$S = \frac{d}{2\tan 2\alpha} \tag{S6}$$

C. MIL with a non-ideal setup

In the following paragraphs we extend the concept of MIL and we study its behavior in the non-ideal scenario where there is an asymmetry in the grazing angles of the two mirrors and a possible wafer misalignment. In the special case shown in Fig. 1b, one could introduce an additional angle component δ on the second mirror. Additionally, the normal vector of the wafer plane could also form an angle θ with the direction of propagation of the incoming beam z (Fig. S2a). The case of $\delta \neq 0$ is very probable and can vary every time new mirrors are glued on the device. To this end, we derive Eq. (S12) that shows the corrected pitch based on the geometrical analysis of Fig. S2b.

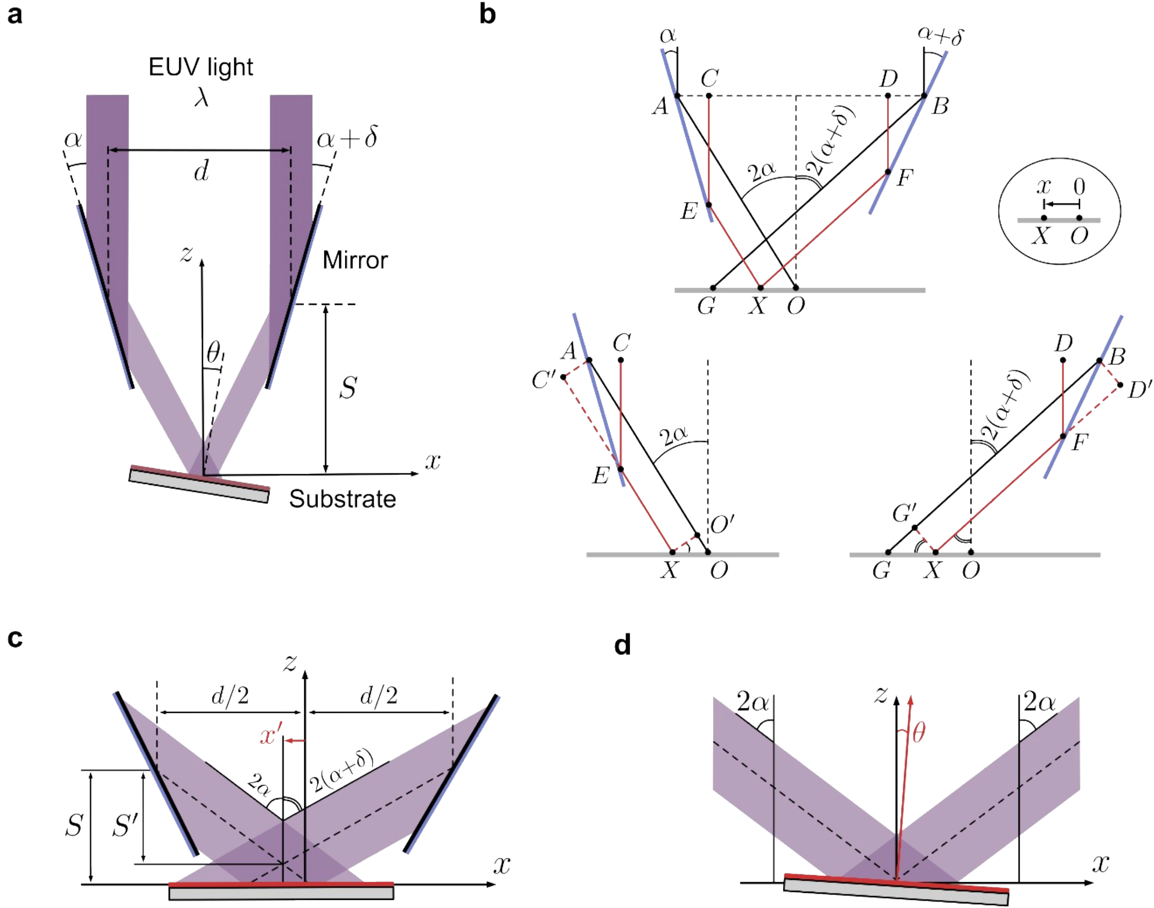

Fig. S2 | Geometrical analysis of MIL. (a) Extended version of Fig. 1b featuring a non-symmetrical case of the MIL device. One of the mirrors has a higher angle than the other by a value δ, and the wafer is tilted at an angle θ. (b) Geometrical analysis of the asymmetric case, in which the difference of the optical path lengths CEX and DFX is expressed as a function of position x and the grazing angles in order to derive the interference pitch. (c) The elevation of the overlap area with respect the sample at the asymmetric case. (d) The tilted-wafer case, in which the pitch is projected at an angle θ leading to an observed pitch expanded by $1/\cos\theta$.

We define as positive δ the angle that increases the value of α. To understand the effect on the patterning pitch, one can express the difference of the optical path lengths of the two beams that interfere at point X of Fig. 2b, CEX and DFX (red lines). We assume that the wavefront reaches the two mirrors at points A and B respectively. The light reflected at point A reaches the wafer plane at point O that we assume as the origin ($x = 0$) and the distance OX can be parametrized as x. We express the optical path lengths $OPD1 = AO - CEX$ and $OPD2 = BG - DFX$ and study them individually in the assistive schematics of Fig. 2b, where we substitute C and D with the virtual sources C' and D', positioned so that $CE = C'E$ and $DE = D'E$.

We now observe that $OPD1 = AO - C^{'}X = OO'$ and $OPD2 = BG - D^{'}X = GG'$ that can be expressed as functions of x and the grazing angles:

$$OO^{'} = x\sin 2\alpha \tag{S7}$$

$$GG' = (OG - x)\sin 2(\alpha + \delta) \tag{S8}$$

The optical path difference between the red lines DFX and CEX is:

$$OPD = DFX - CEX = (BG - OPD2) - (AO - OPD1) = \left(BG - GG^{'}\right) - (AO - OO')$$

Using Eq. (S7) and (S8)

$$OPD = BG - OG\sin 2(\alpha + \delta) + x\sin 2(\alpha + \delta) - AO + x\sin 2\alpha$$

$$OPD = (\sin 2\alpha + \sin 2(\alpha + \delta))x + (BG - AO - OG\sin 2(\alpha + \delta)) \tag{S9}$$

Constructive interference occurs when $OPD = n\lambda$. While constant factor $(BG - AO - OG\sin 2(\alpha + \delta))$ in Eq. (S9) can be neglected because it only offsets the interference pattern, the multiplier of x defines the interference period (pitch) as:

$$P = \frac{\lambda}{(\sin 2\alpha + \sin 2(\alpha + \delta))} \tag{S10}$$

The trigonometric formula $\sin u + \sin v = 2\sin\frac{u + v}{2}\cos\frac{u - v}{2}$ reduce the denominator of Eq. (S10) to:

$$\sin 2\alpha + \sin 2(\alpha + \delta) = 2\sin (2\alpha + \delta)\cos \delta \tag{S11}$$

Combining Eq. (S10) & (S11) one gets the period of MIL for the asymmetric case in Eq. (S12) that reduces to Eq. (S5) for $\delta \approx 0$. This assumption corresponds to any practical misalignment in our system and justifies the use of Eq. (S5).

$$P = \frac{\lambda}{2\sin (2a + \delta)\cos \delta} \tag{S12}$$

The distance S between the reflection point and the interference area is changing as well. Interference happens along the rhomboidal area of beam overlap, which is the reason behind the depth-of-focus tolerance of EUV-IL. However, the ideal device-wafer distance is the one that aligns the overlap center with the sample. We study the case of positive δ in Fig. 2**c** where the center is shifted by x' and its new

distance is S'. These parameters can be expressed as functions of the grazing angles and the mirror spacing in Eq. (S13) and (S14). Adding those and solving for S' gives the corrected distance in Eq. (S15), which reduces to Eq. (S6) for $\delta \approx 0$.

$$\tan\left(2(\alpha + \delta)\right) = \frac{d/2 + x'}{S'} \tag{S13}$$

$$\tan 2\alpha = \frac{d/2 - x'}{S'} \tag{S14}$$

$$S' = \frac{d}{\tan 2\alpha + \tan\left(2(\alpha + \delta)\right)} \tag{S15}$$

A wafer tilt is expected to have a negligible effect even in an experimental setup. We introduce an angle of θ with respect to the ideal wafer normal, as shown in Fig. S2d. According to Eq. (S16) the observed pitch is increased by the projection factor $1/\cos\theta$.

$$P_\theta = \frac{P}{\cos\theta} \tag{S16}$$

D. NILS calculation for monochromatic light

Normalized image log-slope (NILS) characterizes the edge definition of a pattern. It is defined in Eq. (S17)[3] as the intensity slope at the border of the pattern area, normalized by the intensity value at this point and the nominal linewidth of the patterned feature.

$$\mathrm{NILS} = \frac{1}{I}\frac{dI}{dx}w \tag{S17}$$

Plugging Eq. (S4) in Eq. (S17) yields:

$$\frac{1}{I}\frac{dI}{dx}w = -\frac{4\pi}{\lambda}sin(2a)\frac{sin\left(\frac{4\pi}{\lambda}sin(2a)\,x\right)}{1 + cos\left(\frac{4\pi}{\lambda}sin(2a)\,x\right)}w$$

Using the trigonometric identity: $\frac{\sin\theta}{1 + \cos\theta} = \tan\frac{\theta}{2}$

$$\frac{1}{I}\frac{dI}{dx}w = -\frac{4\pi}{\lambda}sin(2a)\ tan\left(\frac{2\pi}{\lambda}sin(2a)\ x\right)w \tag{S18}$$

We calculate NILS for HP lines with width:

$$w = \frac{p}{2} = \frac{\lambda}{4sin(2a)} \tag{S19}$$

Eq. (S19) in Eq. (S18) gives:

$$\frac{1}{I}\frac{dI}{dx}w = -\frac{\lambda}{4\sin(2a)}\frac{4\pi}{\lambda}sin(2a)\ tan\left(\frac{2\pi}{\lambda}sin(2a)\ x\right) = -\pi\ tan\left(\frac{2\pi}{\lambda}sin(2a)\ x\right)$$

Including the pitch from Eq. (S5), NILS expression becomes:

$$\mathrm{NILS} = \frac{1}{I}\frac{dI}{dx}w = -\pi\ tan\left(\frac{\pi}{p}x\right) \tag{S20}$$

We calculate NILS specifically at the borders of the HP lines. Therefore, the positions x are given by the sequence in Eq. (S21) that becomes Eq. (S22) including the pitch Eq. (S5).

$$x = (2n-1)\frac{P}{4},\ n = 1,2,\ldots \tag{S21}$$

$$x = (2n-1)\frac{\lambda}{8sin(2a)},\ n = 1,2,\ldots \tag{S22}$$

Finally, Eq. (S22) in Eq. (S20) gives:

$$\mathrm{NILS} = \frac{1}{I}\frac{dI}{dx}w = -\pi\ tan\left(\frac{2\pi}{\lambda}sin(2a)\ (2n-1)\frac{\lambda}{8\sin(2a)}\right) = -\pi\tan\left(\frac{\pi}{4}(2n-1)\right),\quad n = 1,2,\ldots$$

Signs distinguish the leading from the trailing edges, but NILS is reported as an absolute value, Eq. (S23).

$$\mathrm{NILS} = \left|(-1)^n\pi\right|,\quad n = 1,2,\ldots \rightarrow\ \mathrm{NILS} = \pi \tag{S23}$$

E. Mirror-surface roughness and reflectivity

Surface roughness affects the optical properties of surfaces, particularly reflectivity which defines the efficiency of MIL. A smoother surface typically yields higher reflectivity, as it minimizes scattering and absorption of incident light. We characterized our 10 nm Ru films post deposition via Atomic Force Microscopy (AFM). The obtained topography image (Fig. S3a) was analyzed with WsXM software[4] and the height sensor measurements showed a root mean square (RMS) roughness of 0.15 nm (see Fig. S3b). We simulated[5] the reflectivity at the range of grazing angles that corresponds to our inventory of MIL devices and one can see that the impact of roughness becomes more prominent as the angle increases (see Fig. S3c). It seems that the sub-1 nm RMS roughness has a minimal effect on the reflectance, therefore, we have set the design limit for roughness at 0.5 nm RMS and configured the simulations (Fig. 3 & 6) on this worst-case scenario.

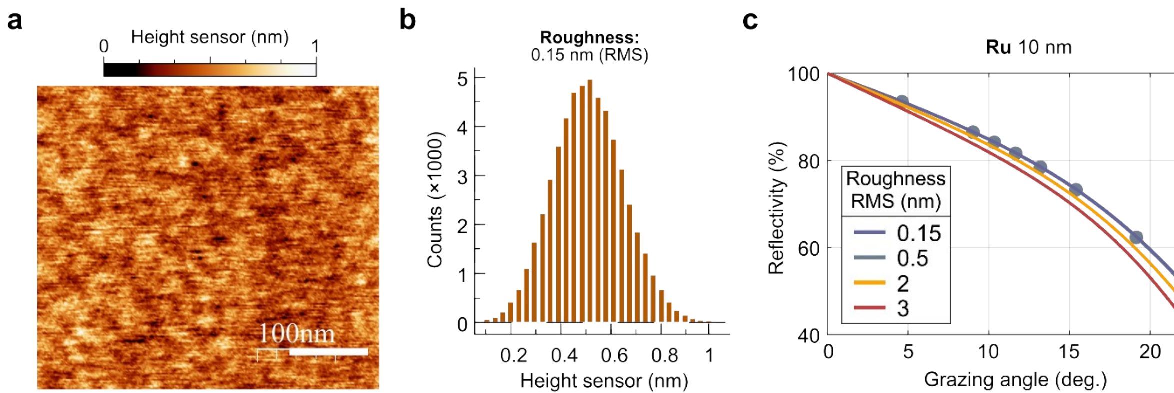

Fig. S3 | Surface roughness in MIL. (a) AFM image of the mirror surface, after Ru 10 nm deposition. (b) The distribution of the corresponding height-sensor measurements that shows an RMS roughness of 0.15 nm. (c) Simulated reflectivity as a function of grazing angle for different roughness values.

References

1 X. Wang, D. Kazazis, L.-T. Tseng, A. P. G. Robinson and Y. Ekinci, *Nanotechnology*, 2021, **33**, 065301.

2 X. Wang, L.-T. Tseng, D. Kazazis, Z. Tasdemir, M. Vockenhuber, I. Mochi and Y. Ekinci, *J. Micro/Nanolith. MEMS MOEMS*, 2019, **18**, 013501.

3 H. J. Levinson, *Principles of lithography*, SPIE Press, Bellingham, 3rd edn., 2010.

4 I. Horcas, R. Fernández, J. M. Gómez-Rodríguez, J. Colchero, J. Gómez-Herrero and A. M. Baro, *Review of Scientific Instruments*, 2007, **78**, 013705.

5 B. L. Henke, E. M. Gullikson and J. C. Davis, *At. Data Nuc. Data Tables*, 1993, **54**, 181-342.